JOURNAL OF GEOPHYSICAL RESEARCH, VOL. 114, D00F07, doi:10.1029/2008JD011604, 2009

Aerosol optical and hygroscopic properties during TexAQS-GoMACCS 2006 and their impact on aerosol direct radiative forcing

P. Massoli,[1,2] T. S. Bates,[3] P. K. Quinn,[3] D. A. Lack,[1,2] T. Baynard,[1,2,4] B. M. Lerner,[1,2] S. C. Tucker,[1,2] J. Brioude,[1,2] A. Stohl,[5] and E. J. Williams[1,2]

Received 8 December 2008; revised 1 February 2009; accepted 17 February 2009; published 16 April 2009.

[1] In situ measurements of aerosol optical and hygroscopic properties were made on board the National Oceanic and Atmospheric Administration R/V *Ronald H. Brown* during the Texas Air Quality Study–Gulf of Mexico Atmospheric Composition and Climate Study (TexAQS-GoMACCS). The aerosol light extinction coefficient (σ_{ep}) was measured at 355, 532, and 1064 nm at 25%, 60%, and 85% relative humidity (RH) for both sub-1- and sub-10-μm-diameter particles with a cavity ring–down aerosol extinction spectrometer. The 532-nm σ_{ep} was coupled with the 532-nm light absorption coefficient (σ_{ap}) measured with a photoacoustic absorption spectrometer to calculate the aerosol single scattering albedo (ω) with absolute uncertainty <0.01. The σ_{ep} dependence on RH was expressed in terms of gamma (γ). The sampled aerosols covered a broad spectrum of γ and ω values; aerosols from traffic emissions were hydrophobic and highly light-absorbing with $\gamma \sim 0.4$ and $\omega \sim 0.6$, whereas the regional aerosols exhibited variable values of both γ and ω. Aerosols with the highest sulfate content also had the highest γ and ω values (>0.65 and >0.9, respectively). The optical data were used to estimate local, top of atmosphere aerosol-induced climate forcing (ΔF_R). The ΔF_R calculations were performed using both ω values measured at 25% RH and ω values converted to ambient RH. The calculated ambient ΔF_R ranged from -7 to -40 W/m^2 with absolute uncertainty between 0.7 and 2.5 W/m^2. The results show that including aerosol hygroscopic properties in climate calculations is critical for improving estimates of aerosol forcing on climate.

Citation: Massoli, P., T. S. Bates, P. K. Quinn, D. A. Lack, T. Baynard, B. M. Lerner, S. C. Tucker, J. Brioude, A. Stohl, and E. J. Williams (2009), Aerosol optical and hygroscopic properties during TexAQS-GoMACCS 2006 and their impact on aerosol direct radiative forcing, *J. Geophys. Res.*, *114*, D00F07, doi:10.1029/2008JD011604.

1. Introduction

[2] The Texas Air Quality Study–Gulf of Mexico Atmospheric Composition and Climate Study (TexAQS–GoMACCS) took place in summer 2006 to identify the sources, transport processes, and radiative properties of aerosols over the Gulf of Mexico and the Houston/Galveston area. The NOAA research vessel *Ronald H. Brown* (RHB) spent approximately 5 weeks in this region (2 August thru 11 September 2006) with a number of gas and aerosol instruments deployed to measure air quality and climate relevant parameters. The Houston metropolitan area and surrounding region are heavily industrialized and urbanized, and they often experience high mass concentrations of particulate matter with diameters <2.5 μm, or $PM_{2.5}$ [*Allen and Fraser*, 2006] and high ozone levels [*Kleinman et al.*, 2002]. Typical industrial activities in the area include refineries, petrochemical facilities and power plants, with emissions rich in reactive volatile organic compounds (VOCs) and NO_X [*Ryerson et al.*, 2003, and references therein]. In this environment, secondary organic aerosol (SOA) resulting from gas-to-particle conversion of VOCs are likely to constitute a substantial fraction of the aerosol organic mass [*de Gouw et al.*, 2005; R. Bahreini et al., Organic aerosol formation in urban and industrial plumes near Houston and Dallas, Texas, submitted to *Journal of Geophysical Research*, 2008]. Similarly, high concentrations of sulfate aerosols are expected from the oxidation of SO_2 that is emitted by diesel-fueled mobile sources and from the numerous coal-fired industries and power generation stations located both in the Houston area and elsewhere in Texas [*Brock et al.*, 2003; *Bates et al.*, 2008]. On the basis of 2006 emission inventories around 0.1 Tgr a^{-1} of SO_2 are emitted in the Houston region (G. Frost, personal communication, 2008, http://www.tceq.

[1]Cooperative Institute for Research in Environmental Sciences, University of Colorado, Boulder, Colorado, USA.
[2]Chemical Sciences Division, Earth System Research Laboratory, NOAA, Boulder, Colorado, USA.
[3]Pacific Marine Environment Laboratory, NOAA, Seattle, Washington, USA.
[4]Now at Lockheed Martin Coherent Technologies, Louisville, Colorado, USA.
[5]Department of Regional and Global Pollution Issues, Norwegian Institute for Air Research, Kjeller, Norway.

0148-0227/09/2008JD011604$09.00

state.tx.us/implementation/air/industei/psei/psei.html). The heavy commercial vessel traffic in the area is also a significant source of SO_2 (E. J. Williams et al., Emissions of NO_X, CO, SO_2, H_2CO and C_2H_4 from commercial marine vessels during TexAQS 2006, manuscript in preparation, 2009) and particulate matter including black carbon or soot [*Lack et al.*, 2008, 2009]. The Houston/Galveston area experiences substantial air quality degradation especially in summertime, when photochemistry is at its maximum and land/sea breezes favor air stagnation in Galveston Bay and along the Texas coastline [*Banta et al.*, 2005]. These conditions lead to frequent episodes of elevated surface ozone concentrations, with summer daytime levels often exceeding the U.S. national ambient air quality standards [*Zhang et al.*, 2004].

[3] Accurate measurements of aerosol optical properties (light extinction coefficient (σ_{ep}), light scattering coefficient (σ_{sp}) and light absorption coefficient (σ_{ap})) are necessary to calculate particle single scattering albedo (ω) and estimate direct aerosol radiative forcing on climate. Aerosol optical properties can be strongly dependent upon relative humidity (RH). Water uptake affects aerosol atmospheric lifetime and composition, which in turn affect atmospheric visibility, direct radiative forcing of climate [*Intergovernmental Panel on Climate Change* (*IPCC*), 2007] and cloud microphysics [*Lohmann and Feichter*, 2005]. The dependence of σ_{ep} (or σ_{sp}) on relative humidity, $f\sigma(RH)$, is determined empirically by simultaneous measurements of σ_{ep} (or σ_{sp}) at two different RH values, typically at a high (RH > 75%) and a low (RH < 40%) value. Many studies have reported the humidity response of both laboratory-generated and atmospheric aerosols [*Doherty et al.*, 2005; *Baynard et al.*, 2006; *Garland et al.*, 2007] and empirically derived $f(RH)$ are now incorporated into most chemical transport and radiative transfer models; however, some difficulties still exist in modeling the changes of aerosol optical responses with water uptake for species such as dust and soot, and in generalizing the treatment of complex organic aerosols [*Malm and Kreidenweis*, 1997; *Kanakidou et al.*, 2005; *Mircea et al.*, 2005]. Furthermore, most satellite algorithms retrievals still widely omit hygroscopic properties of ambient aerosols [*Bates et al.*, 2006; *Wang and Martin*, 2007]. Recent work has provided empirically based parameterizations to generalize and simplify the treatment of the RH dependence of σ_{ep} (or σ_{sp}) as function of aerosol size, composition and mixing state [*Malm et al.*, 2005; *Quinn et al.*, 2005].

[4] This paper reports the in situ optical and hygroscopic aerosol properties measured onboard RHB using a three-wavelength cavity ring-down aerosol extinction spectrometer, CRD [*Baynard et al.*, 2007] and a photoacoustic aerosol absorption spectrometer, PAS [*Lack et al.*, 2006]. The CRD was configured to provide 532 nm σ_{ep} measurements at 25%, 65% and 85% RH, and 355 and 1064 nm σ_{ep} measurements at 25% and 85% RH. The PAS measured the σ_{ap} coefficient at 532 nm and 25% RH, which was used with measurements from the CRD to obtain ω. A detailed description of the optical measurements is given in section 2. The measured and derived aerosol optical properties are evaluated in the context of the aerosol chemical composition and meteorology to better understand the factors affecting the optical properties (section 3). We find that both the specific meteorological conditions of the area and episodes of long-range transport can play a decisive role in impacting the region air quality. Finally, in section 4 we use the measured optical parameters in simple radiative forcing calculations to estimate the aerosol-induced forcing (ΔF_R) at the top of atmosphere (TOA). We quantify the uncertainty in forcing on the basis of current measurement uncertainties of the experimental ω obtained from the CRD and PAS, and demonstrate the sensitivity of radiative forcing to the uncertainty in the ω measurements. By performing these calculations using both the measured ω values (25% RH) and ω values adjusted to ambient RH, we show the sensitivity of forcing to changes in relative humidity.

2. Instruments and Methods

2.1. Aerosol Sampling

[5] Air was sampled 18 m above sea level through a 6-m-long mast drawing 1 m^3/min of air into the laboratory container. The mast was positioned forward of the ship's stack and automatically pointed into the relative wind to maximize sampling efficiency and avoid RHB's exhaust. The mast was heated in its lowest 1.5 m to reduce the RH to ~60%. Further details about the sampling mast are given by *Bates et al.* [2002]. At the bottom of the mast, several 1.6 cm inner diameter conductive tubes were used to supply 30 L/min flow to the instruments used for aerosol optical, chemical and physical measurements. Upstream of the CRD, an automated, computer controlled valve switched the sample flow between two Berner-type impactors [*Berner et al.*, 1979] to select either sub-10- or sub-1-μm-diameter particles (aerodynamic 50% cutoff diameter). Flexible conductive silicone tubing (TSI Inc.) was used between the impactor and CRD to avoid sharp bends. On the basis of previous laboratory studies with the same setup, losses through the inlet feeding the CRD were insignificant for sub-1-μm-diameter particles, and <2% for 1- to 5-μm-diameter particles. In this paper, we report only the measurements of sub-1-μm aerosols.

2.2. Aerosol Optical Instrumentation

[6] The CRD was equipped with six channels for measurements of σ_{ep} at different RH values. The σ_{ep} at 532 nm was measured at 25%, 60% and 85% RH (three separated CRD cavities with independent flow and RH control). The 355 and 1064 nm CRD cavities were connected in series, with the upstream aerosol flow alternating between 25% and 85% RH. The 85% RH was reached by natural cooling of the sample stream when moving from the heated mast (~32°C, 60% RH) to the CRD cavities insulated at the laboratory temperature (~25°C). The midpoint RH (60%) was obtained by heating a second 532-nm CRD cell to ~32°C. For the measurements at 25% RH, the flow was dried by passing the sample air through Nafion diffusion driers (Permapure Inc.). These RH values were stable through the experiment (standard deviation of ±3% RH). Temperature was monitored in several critical points of the CRD, and the RH values were measured either immediately downstream or inside each CRD cavity. Humidity in the 85% and 25% RH cavities was measured using high-precision Rotronics probes (Rotronics Inc.) having an accuracy of ±0.5°C and ±1% RH. RH in the other cavities was measured by Vaisala probes (Vaisala Inc.) with accuracy ±2% RH. The probes were checked after the

field mission, and minimal drift was found from the previous calibration. RH was also calculated in each CRD cavity using temperature measured with thermistors (Omega Inc.).

[7] A fourth CRD cavity measured particle free air to determine the interference from gas phase species at 532 nm, mainly NO_2 [*Baynard et al.*, 2007]. Gas phase interference contributed, on average, 4% to σ_{ep} and 15% to σ_{ap}, and was subtracted from total aerosol extinction and total absorption. For 1-min time resolution, the uncertainty in the submicrometer σ_{ep} at 532 nm and 25% RH was $\delta\sigma_{ep}$ = 1%. For measurements at elevated RH levels, the $\delta\sigma_{ep}$ was generally higher mostly owing to the uncertainty in the measured RH values. With an average accuracy of ±1% RH, $\delta\sigma_{ep}$ was approximately 5% and 2% for measurements at 85% and 60% RH, respectively.

[8] We express the RH dependence of σ_{ep} at 532 nm,

$$\gamma_{ep} = \frac{\log\left(\sigma_{ep}RH/\sigma_{ep}RHref\right)}{\log(100 - RHref) - \log(100 - RH)}, \quad (1)$$

where in our study *RHref* is 25% RH. The γ parameter in our case was obtained by combining the three σ_{ep} measurements at 85%, 65% and 25% RH. The use of γ has the advantage of describing the hygroscopic behavior of aerosols in a linear manner over a broad range of RH values; it also implies that particles are deliquesced [*Quinn et al.*, 2005], a reasonable assumption for this data set due to the high ambient relative humidity during the field study. The γ parameter is dimensionless, and it increases with increasing particle water uptake. From previous studies, typical values of γ for ambient aerosol ranged between 0.1 and 1.5 [*Gassó et al.*, 2000; *Quinn et al.*, 2005; *Clarke et al.*, 2007]. The absolute uncertainty in the γ values reported in this work, $\delta\gamma$, is ~0.03 for submicron sizes and 1 min or longer averaging times.

[9] The values of 355- and 1064-nm submicrometer σ_{ep} at 25% RH were used to calculate the Ångström exponent of light extinction ($\mathring{A}\sigma_{ep}$) according to [*Ångström*, 1929]

$$\dot{\mathrm{A}}\sigma_{ep,\lambda1,\lambda2} = -\frac{\ln\left(\sigma_{ep,\lambda_1}/\sigma_{ep,\lambda_2}\right)}{\ln\left(\lambda_1/\lambda_2\right)}, \quad (2)$$

where λ_1 = 355 nm and λ_2 = 1064 nm. The absolute uncertainty in $\mathring{A}\sigma_{ep}$ is 0.02 based on $\delta\sigma_{ep}$ values of 1.5% for the 355 and 1064 nm σ_{ep} measured at 25% RH and for sub-1-μm sizes, signal levels >5 Mm^{-1}, and time resolution of 1 min or higher. We also report $\mathring{A}\sigma_{ep}$ for ambient RH conditions ($\mathring{A}\sigma_{ep\_ambient}$), obtained using the 355- and 1064-nm σ_{ep} data converted to ambient RH by using the $f\sigma_{ep,355}(RH)$ and the $f\sigma_{ep,1064}(RH)$ as scaling factors, respectively. The absolute uncertainty in $\mathring{A}\sigma_{ep\_ambient}$ is 0.08 based on a 5% $\delta\sigma_{ep}$ value for the 355- and 1064-nm σ_{ep} coefficients converted to ambient RH.

[10] The σ_{ap} was inferred by PAS on the basis of aerosol light absorption technique (PAS), which provides a measure of the actual heat released by particles from the absorption of power modulated light. The heat release creates a pressure wave that resonates in a frequency modulated cavity and it can be detected as a sound wave; the acoustic response is in turn converted into particle light absorption response. Further details of the PAS instrument and principles are described by *Lack et al.* [2006]. The PAS was connected downstream of the CRD and measured the sub-1-μm σ_{ap} at 532 nm and 25% RH with an estimated uncertainty of 5%. Combination of the 532-nm σ_{ep} and σ_{ap} at 25% RH provided a direct measure of ω as

$$\omega = \frac{\sigma_{ep} - \sigma_{ap}}{\sigma_{ep}}. \quad (3)$$

The absolute uncertainty for the ω values measured at 25% RH ($\delta\omega$) is estimated by propagating the uncertainty of the independent values $\delta\sigma_{ep}$ = 1% and $\delta\sigma_{ap}$ = 5%. The $\delta\omega$ values varied with ω from 0.01 (for ω = 0.8) to 0.03 (for ω = 0.4). Values of ω are also reported for ambient RH conditions ($\omega_{ambient}$), using σ_{ep} converted to ambient RH and assuming σ_{ap} is not a function of RH [*Nessler et al.*, 2005]. The uncertainty in the ambient ω values ($\delta\omega_{ambient}$) is based on $\delta\sigma_{ep}$ = 5% and $\delta\sigma_{ap}$ = 5%, and is $\delta\omega_{ambient}$ = 0.015 (for ω = 0.8), and 0.042 (for ω = 0.4). All parameters are reported at 298 K and 1013.25 hPa.

2.3. Aerosol and Gas-Phase Chemistry Measurements

[11] Nonrefractory (NR) aerosol chemical composition was measured onboard RHB with a quadrupole aerosol mass spectrometer (Q-AMS, Aerodyne Research Inc., Billerica, Massachusetts) [*Jayne et al.*, 2000]. The Q-AMS provides concentrations in $\mu g\ m^{-3}$ of NR NH_4^+, SO_4^{2-}, NO_3^- and POM (particulate organic matter). Details of the Q-AMS performance and operation during TeXAQS-GoMACCS are reported by *Bates et al.* [2008]. The SO_4^{2-} and POM concentrations were used to calculate the parameter F_{POM}, as

$$F_{POM} = \frac{POM}{POM + SO_4^{2-}}, \quad (4)$$

where the sum of POM and SO_4^{2-} is assumed to represent the majority of the submicrometer aerosol mass [*Quinn et al.*, 2005]. The hydrocarbon-like (HOA) and the oxygenated (OOA) organic aerosol fractions based on the m/z of 57 and 44, respectively [*Zhang et al.*, 2005] were used to calculate F_{OOA},

$$F_{OOA} = \frac{OOA}{OOA + HOA}, \quad (5)$$

where the reconstructed sum of OOA and HOA concentrations is approximately equal to NR POM [*Bates et al.*, 2008].

[12] Tropospheric ozone mixing ratios (O_3, ppb) were measured with two commercial TECO 49 instruments, calibrated with a NIST traceable standard prior to the field experiment. The O_3 detection limit was 2 ppbv with a 10-s time resolution. Carbon monoxide (CO, ppbv) was measured via vacuum UV fluorescence with a commercial CO analyzer (AL 5002, AeroLaser GmbH, Germany). The CO detection limit was 1.5 ppbv for 1-Hz data averaged to 1-min time resolution. Sulfur dioxide (SO_2, ppbv) was measured with a pulsed UV fluorescence analyzer (Thermo Environmental Instruments[1], TEI, Model 43C) with a detection limit of

100 pptv with a 1-min time resolution. Measured concentrations of SO_2 and NR SO_4^{2-} were used to calculate the fraction of sulfur as sulfate, F_{SO4},

$$F_{SO4} = \frac{SO_4^{2-}}{SO_4^{2-} + SO_2}. \quad (6)$$

F_{SO4} is an indicator of the level of aerosol "relative age" or oxidation in absence of significant fresher emissions [*Quinn et al.*, 2005], with higher F_{SO4} indicating older aerosols due to oxidation of SO_2 into SO_4^{2-}. The use of F_{SO4} as an indicator of aerosol relative age in the TeXAQS-GoMACCS study region was limited by the existence of both onshore and offshore sources of SO_2 and SO_4^{2-}. However, F_{SO4} remains useful as a qualitative indicator of the aerosol oxidation level. High F_{SO4} values unambiguously indicate that the aerosol is oxidized and there were no recent inputs of SO_2. A low F_{SO4} value is more ambiguous, because it might indicate either recent addition of SO_2 to an aged aerosol or recent emission of SO_2 that has not yet oxidized to SO_4^{2-}. We also use measurements of NR NH_4^+, NO_3^- and SO_4^{2-} to estimate the degree of aerosol neutralization (or acidification) defined as the equivalence ratio (ER),

$$ER = \frac{NH_4^+}{NO_3^- + 2 * SO_4^{2-}}. \quad (7)$$

Aerosol optical depth (AOD) was measured using three five-channel handheld Microtops Sun photometers (Solar Light Co., units SN 4080, 3803 and 5355) at wavelengths of 340, 380, 440, 500, 675, and 870 nm [*Quinn et al.*, 2002]. The Sun photometers were calibrated prior to the field deployment. Data reduction followed the protocol of *Knobelspiesse et al.* [2003]. Ozone column amounts used to calculate the ozone optical depth were obtained from daily ozone sondes launched from the ship. AOD was measured on RHB twice a day between 1000 and 1400 local standard time during periods of clear sky. The absolute uncertainty for AOD values is 0.015.

2.4. FLEXPART and Mixing Height Estimates

[13] The Lagrangian dispersion model for particle transport and diffusion FLEXPART version 6.2 [*Stohl et al.*, 1998, 2005] provides air mass transport pathways and information regarding how anthropogenic emissions of CO, NO_X and SO_2 are likely to impact such air masses. FLEXPART backward transport simulations were calculated for each hour along the RHB cruise track or whenever the ship changed position by more than 0.1 degrees in either latitude or longitude. Each simulation results from 40,000 particles being released in a certain volume of sampled air and transported back in time. The spatial distribution of the air mass in the day(s) prior to sampling, expressed as its sensitivity to emission input, is given with 1-day resolution [*Seibert and Frank*, 2004]. FLEXPART uses meteorological input data from the European Centre for Medium Range Weather Forecast (ECMWF) provided with standard resolution of $0.36° \times 0.36°$. Current emission inventories are used to estimate the contribution of anthropogenic sources emitted into the modeled air parcels. The FLEXPART product used here is the footprint emission sensitivity (ns kg^{-1}) which is a measure of the residence time of the particles in the lowest 100 m of the vertical column mapped at a resolution of $0.1° \times 0.1°$. Additional information on the FLEXPART model and other output products are described at http://transport.nilu.no/flexpart.

[14] Higher-resolution FLEXPART backward simulations were also made available by using the meteorological field outputs from the Weather Research and Forecasting (WRF) model [*Doran et al.*, 2008] with a horizontal resolution of 5 km and 60 vertical levels. In this case, the simulations are based on 20,000 particles released every 15 min from boxes of 20 by 20 km in horizontal size and 100 m in vertical size, and centered along the RHB pathway. The FLEXPART output grid had a resolution of 5 km, and included a turbulent parameterization based on the turbulent kinetic energy from WRF.

[15] NOAA's high-resolution Doppler lidar (HDRL) provided detailed information about three-dimensional wind speed and direction as well as turbulence profiles from which mixing heights could be estimated following the procedure described by *Tucker et al.* [2009].

2.5. Meteorological Conditions During TexAQS–GoMACCS

[16] The RHB cruise tracks in the Gulf of Mexico and the various locations sampled during the study are shown in Figure 1a. Figure 1b depicts the ship track in Galveston Bay and along the industrial ship channel, and the location of Barbours Cut, a container port at the south entrance of the ship channel where the RHB spent ~200 h during the study.

[17] Southerly winds with either westerly or easterly components (ESE-WSW) were the prevailing synoptic meteorological condition until late August. Under these conditions, the submicrometer aerosol was largely from local sources with variable aerosol amounts and composition depending on wind direction and sampling location. Occasionally, the Galveston Bay meteorology was dominated by the local land/sea breeze circulation typical of this area in summer. From late August into mid September, air masses came predominantly from the continental United States owing to stronger northerly winds often with an easterly component (N-NE). The aerosols in these air masses were mixtures from local urban/industrial sources; rural sources in Texas, Arkansas and Louisiana; and distant sources in the northeast United States.

[18] The marine boundary layer height was highly dependent on location and time; it extended to 500–600 m without a diurnal cycle offshore in the Gulf of Mexico, whereas inland it ranged from 200 m during the night to 800 to 1200 m during the day. *Bates et al.* [2008] demonstrated that the daily variation in mixing height had a primary role in shaping the composition of the surface aerosol in the Galveston Bay area, to the point that daily trends observed in the aerosol composition could be largely explained by vertical mixing of aerosol precursors and particles emitted and mixed at different times of the day.

3. Results: Aerosol Optical Properties and Source Apportionment

[19] The aerosols sampled on RHB during TexAQS were extremely diverse owing to the large number of nearby urban

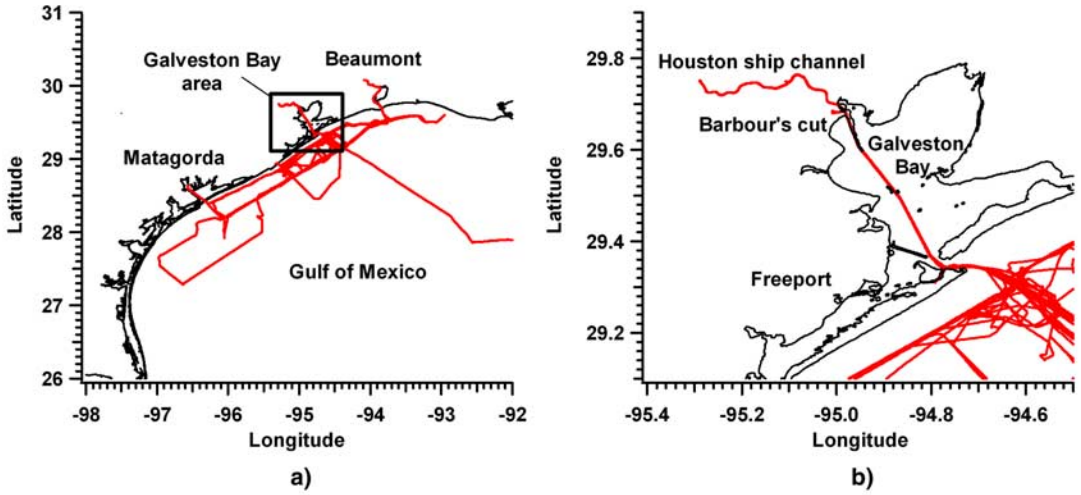

Figure 1. (a) *Ronald H. Brown* cruise track in the Gulf of Mexico during the period 2 August to 11 September 2006. (b) Enlarged map of Galveston Bay.

and industrial sources of particles and particle precursors, many different regional sources, long-range transport, and the complex meteorological patterns associated with the coastal geography of the Houston area. *Bates et al.* [2008] and D. Covert et al. (Aerosol optical properties in the Texas Gulf coast region during TexAQS-GoMACCS 2006, manuscript in preparation, 2008) describe the chemical and optical properties of the TexAQS-GoMACCS aerosols sampled within three broad air mass categories identified as southerly flow (ESE to WSW) Gulf, southerly flow inland, and northerly flow (WNW to ENE). In the analysis presented here, we focus on portions of the data that are associated with identifiable sources and with specific aerosol characteristics (Table 1). For each of these case studies we report the optical and chemical properties of the aerosol (γ, ω, the organic fraction F_{POM} and the oxygenated organic fraction F_{OOA}), and gas phase parameters used for source apportionment (Table 2).

3.1. Urban Traffic Emissions

[20] RHB was often stationed overnight in Barbours Cut, south of the industrial ship channel (Figure 1b). A highway that crosses the ship channel approximately 1.6 km west of Barbours Cut was directly upwind of RHB on 13–15 August during the early morning hours, when the boundary layer was shallow and fresh emissions were confined to near the surface. Figure 2a shows time series of wind direction (degrees), 25% RH submicron σ_{ep} coefficient (Mm^{-1}), CO (ppbv) and NO_2 (ppbv) for this period. On 14 and 15 August, the CO, NO_2 and σ_{ep} levels began to increase around 1100 UTC (0600 local time) under westerly winds (250°), peaked between ~1200 and 1300 UTC (~0700–0800 local time) and decreased to previous levels by 1400 UTC (0900 local time). Such evolution is consistent with traffic emissions from the upwind highway. The lack of similar CO and NO_x plumes on a Sunday (13 August) supports this interpretation. The optical (γ, ω), physical ($\mathring{A}\sigma_{ep}$) and chemical (F_{POM}, F_{OOA}) properties of the aerosols associated with the traffic emissions averaged over three episodes (14, 15 August and 3 August, not shown in the time series) are depicted in Figure 2b. The aerosol sampled during morning rush hour shows strong hydrophobic and absorbing properties, with $\gamma <$ 0.6 and $\omega < 0.8$. The lowest γ and ω values (0.3 and 0.5, respectively) occur at the peak of the rush-hour plume between ~1200 and ~1300 UTC. The $\mathring{A}\sigma_{ep}$ values decrease from 1.8 at the beginning of rush hour to 1.3–1.4 at the peak, and then rise again to 1.7 by 1400 UTC. Such a trend in the $\mathring{A}\sigma_{ep}$ values suggests a shift in the particle size toward larger diameters (not due to humidity effect) during the period of maximum traffic impact. Simultaneously measured number size distribution data, not shown here, indicate a significant increase in the number of particle in the 150- to 300-nm-diameter size range during the traffic peak, while sub-100-nm particles were continuously elevated during this period. These results are consistent with previous studies that report accumulation mode soot components (i.e., absorbing and hydrophobic) associated with vehicle traffic [*Imhof et al.*, 2006, and references therein]. Particle composition was dominated by POM, with F_{POM} increasing from ~0.45 (1100 UTC) to 0.7 (1200–1300 UTC) and decreasing back to 0.5 by 1400 UTC. The F_{OOA} values were ~0.3 and did not show significant variations, suggesting that the POM during the rush hours was mostly in the form of hydrocarbon-like organics (HOA) as expected for fresh and relatively unprocessed vehicular sources.

3.2. Air Masses in Galveston Bay

[21] RHB spent a significant amount of time transiting Galveston Bay between Barbours Cut and the Gulf of Mexico to sample air masses transported downwind of Houston and the surrounding industrial centers. On five consecutive days spent in this area (14–18 August), the local meteorology was mostly dominated by the typical offshore land breeze in the morning (northerly to easterly winds) and onshore sea breeze in the afternoon (southeasterly). Previous studies have demonstrated that this recirculation pattern can significantly increase pollutant concentrations in the Houston/Galveston Bay area [*Banta et al.*, 2005]. Figure 3a shows the time series of wind direction, 25% RH submicron σ_{ep} coefficient, CO and O_3 between 14 August 0600 UTC and 18 August 1400 UTC. The wind direction varied daily from westerly

Table 1. Meteorological Conditions, Ship Position, and Upwind Source Region for the Case Studies Described in Section 3

	Time Period (Day, UTC)	Wind Direction	Ambient RH, %	Mixing Height	RHB Location	Air Mass Source
Traffic emissions	3,14,15 August 1100–1400	W (250°)	80	200 m	Barbours Cut	Local Highway
Galveston Bay, 1	14 August 1600–2400	W-E-SW (250°–100°–200°)	70	250 m (1500 UTC) 1300 m (1800 UTC)	Barbours Cut	Urban/Industrial
Galveston Bay, 2	15 August 1600–2400	W-E-SW (250°–100°–200°)	70	250 m (1500 UTC) 1300 m (1800 UTC)	Galveston Bay	Urban/Industrial
Galveston Bay, 3	16–17 August 1500–0130	W-E-SW (300°–100°–200°)	70	400 m (1500 UTC) 800 m (1800 UTC)	Galveston Bay	Urban/Industrial
Galveston Bay, 4a	17 August 1500–2400	N-SE (0°–150°)	65	400 m (1500 UTC) 800 m (1800 UTC)	Galveston Bay	Urban/Industrial
Galveston Bay, 4b	18 August 0000–1300	N-E (0°–100°)	75	500–700 from 0000 until 1300 UTC	Gulf, Galveston Island	Local SO_2 Source
Long-range transport	2 September, 2100 5 September, 0830	N-NE (20°–100°)	70	~600 m	Gulf	Ohio River Valley
Industrial air masses	several days (200 h total)	NE (40°–100°)	70	Variable	Barbours Cut	Industrial

Table 2. Average Values and 1σ Standard Deviations of γ, ω, F_{POM}, F_{OOA}, F_{SO4}, ER, $\mathring{A}\sigma_{ep}$, and $\mathring{A}\sigma_{ep\_ambient}$ During the Case Studies[a]

	Traffic Emissions	Galveston Bay, 1	Galveston Bay, 2	Galveston Bay, 3	Galveston Bay, 4a	Galveston Bay, 4b	ORV	Industrial
CO (ppbv)	300	120	120	140	200	150	200	150–200
O_3 (ppbv)	<10	40	60	80	115	95	90	50–100
γ	0.39 ± 0.08	0.46 ± 0.14	0.57 ± 0.10	0.60 ± 0.05	0.56 ± 0.04	0.73 ± 0.06	0.66 ± 0.07	0.55 ± 0.08
ω	0.60 ± 0.12	0.56 ± 0.17	0.80 ± 0.11	0.81 ± 0.07	0.89 ± 0.04	0.94 ± 0.02	0.93 ± 0.18	0.87 ± 0.10
F_{POM}	0.59 ± 0.09	0.40 ± 0.06	0.42 ± 0.16	0.44 ± 0.07	0.54 ± 0.04	0.34 ± 0.05	0.37 ± 0.06	0.57 ± 0.14
F_{OOA}	0.28 ± 0.01	0.52 ± 0.12	0.65 ± 0.20	0.76 ± 0.13	0.84 ± 0.07	0.92 ± 0.05	0.90 ± 0.04	0.70 ± 0.18
$\mathring{A}\sigma_{ep}$	1.6 ± 0.2	1.65 ± 0.2	1.82 ± 0.2	2.05 ± 0.13	2.22 ± 0.12	2.40 ± 0.18	2.0 ± 0.16	2.05 ± 0.25
$\mathring{A}\sigma_{ep\_ambient}$	n/a	1.76 ± 0.2	1.87 ± 0.14	1.98 ± 0.26	1.90 ± 0.15	2.0 ± 0.17	1.80 ± 0.15	1.99 ± 0.17
F_{SO4}	0.23 ± 0.30	0.36 ± 0.24	0.34 ± 0.25	0.32 ± 0.14	0.36 ± 0.15	0.53 ± 0.18	0.64 ± 0.18	0.30 ± 0.20
ER	0.95 ± 0.19	0.68 ± 0.20	0.71 ± 0.18	0.69 ± 0.17	0.75 ± 0.11	0.41 ± 0.10	0.53 ± 0.08	0.90 ± 0.24

[a]The values of CO and O_3 (ppb) are the peak values reached during those events.

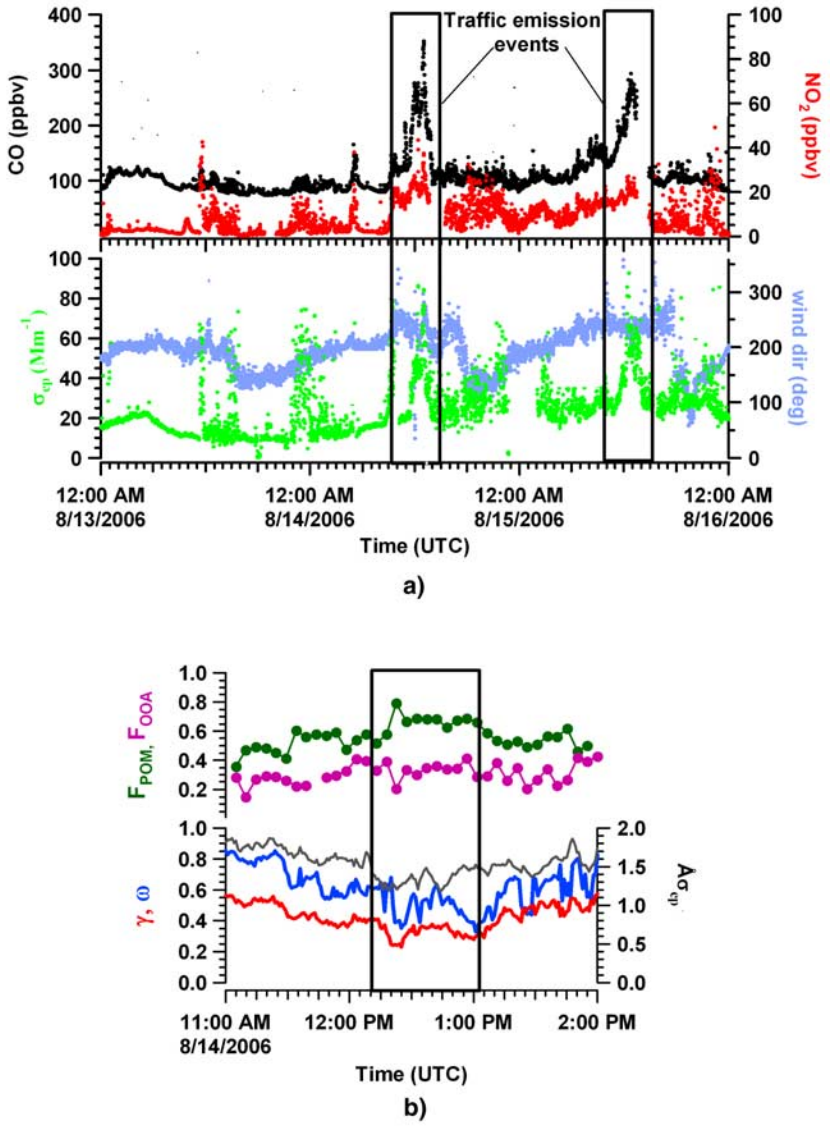

Figure 2. (a) Time series of CO, NO_2, 25% RH σ_{ep} and wind direction from 13–15 August when RHB was in Barbours Cut. Boxed regions indicate traffic emissions sampled during morning rush hours; 13 August was a Sunday with much lighter traffic and it is not included in the analysis. (b) Time series of the average ω, γ, $\text{Å}\sigma_{ep}$, F_{POM}, and F_{OOA} values during 3, 14, and 15 August.

(300°) at 1500 UTC, to easterly (100°) at 1800 UTC and back to southwesterly (200°) at approximately 2100 UTC. The Doppler lidar data (not shown) indicate that the offshore winds were light on 14 and 15 August and stronger on 16 and 17 August. Afternoon return flow was light on all four days. On the night of 17 August, winds were particularly light (<5 m/s), contributing to stagnation at the surface. Dates 15, 16 and 17 August were also characterized by very weak nighttime winds above the shallow nocturnal boundary layer, a condition that allows pollutants and precursors to persist aloft until the next day when they can be mixed down with fresh nighttime–early morning emissions.

[22] Ozone levels increased each day between ~1500 and 2400 UTC (1000–1900 local time) as a result of daily photochemistry [e.g., *Trainer et al.*, 2000]. Afternoon O_3 mixing ratios increased gradually over the five day period from 40 ppbv on 14 August to 115 ppbv on 17 August. After 1600 UTC on 17 August ozone levels were sustained above 75 ppbv for ~11 h. Carbon monoxide levels remained between 100 and 150 ppbv for the first three days, and were higher (200 ppbv) and more variable on 18 August. The submicron σ_{ep} levels associated with the periods of elevated ozone (hereafter periods 1, 2, 3 and 4 as highlighted in Figure 3a) were between 25 and 40 Mm^{-1} in the first three periods, but were substantially higher (45 to 65 Mm^{-1}) during period 4. The properties of the aerosols during these events are shown in Figure 3b. On days with a weak land breeze and relatively low ozone (periods 1 and 2), the optical properties of the aerosols were variable but typical of a relatively unoxidized air mass; aerosols were not hygroscopic (γ = 0.46 and 0.57, respectively) and were absorbing (ω = 0.56 and 0.8, respectively). POM and sulfate contributed roughly equally to the submicron particle mass ($F_{POM} \sim 0.4$). During period 1 the fraction of organic mass that was

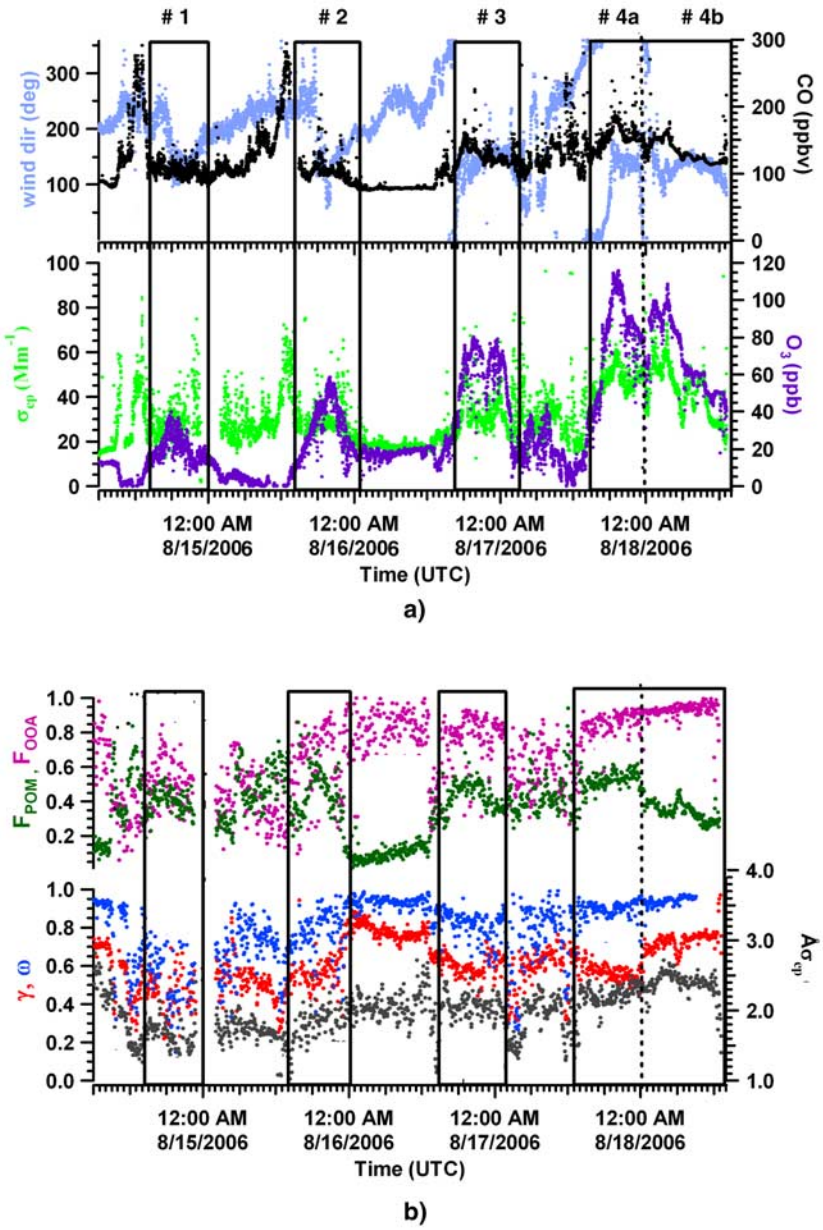

Figure 3. (a) Time series of CO, O_3, 25% RH σ_{ep}, and wind direction from 14–18 August when air masses were sampled in Galveston Bay. Boxed regions are discussed in the text. (b) Time series of γ, ω, Åσ_{ep}, F_{POM}, and F_{OOA} for these events.

oxygenated (F_{OOA}) was ~0.5, while during period 2 F_{OOA} was ~0.65. During periods 3 and 4 (afternoons on 16 and 17 August, respectively), the aerosol was more hygroscopic and the organics were more oxygenated, with $\gamma > 0.55$, $\omega > 0.80$, and $F_{OOA} > 0.8$.

[23] Around 0000 UTC on 18 August, while the ship transited the southern end of Galveston Bay toward the Gulf, a sudden and substantial change occurred in aerosol properties: F_{POM} suddenly decreased from 0.54 to 0.34 and γ increased from 0.56 to 0.73. F_{OOA} and ω gradually increased toward higher values as well. These changes were likely due to a shift in the sampled air mass. Around 2345 UTC on 17 August, preceding the substantial changes observed in the aerosol properties, the wind direction shifted by 360° counterclockwise; Doppler lidar observations show a rapid increase in the mixing height (from ~500 m to ~1500 m), and deep turbulent mixing around the same time. The high-resolution WRF-FLEXPART footprint emission sensitivity shows air mass transport from the west edge of Galveston Bay coming to RHB around 0000 UTC on 18 August (Figures 4a and 4b), and then wrapping around Galveston Bay afterward (Figure 4c). After this time, both HRDL and FLEXPART show greater transport from the east side of Galveston bay rather than the west edge.

[24] A broad increase in SO_2 (up to 10 ppbv) was observed after 0000 UTC with two more concentrated plumes reaching mixing ratios of 25 ppbv at 0130 and 0300 UTC (Figure 4d). During this same period, sulfate aerosol concentrations increased to ~10 μg m^{-3}, with a peak at 0300 UTC of ~17 μg m^{-3}. The CO and CO_2 traces correlate well with

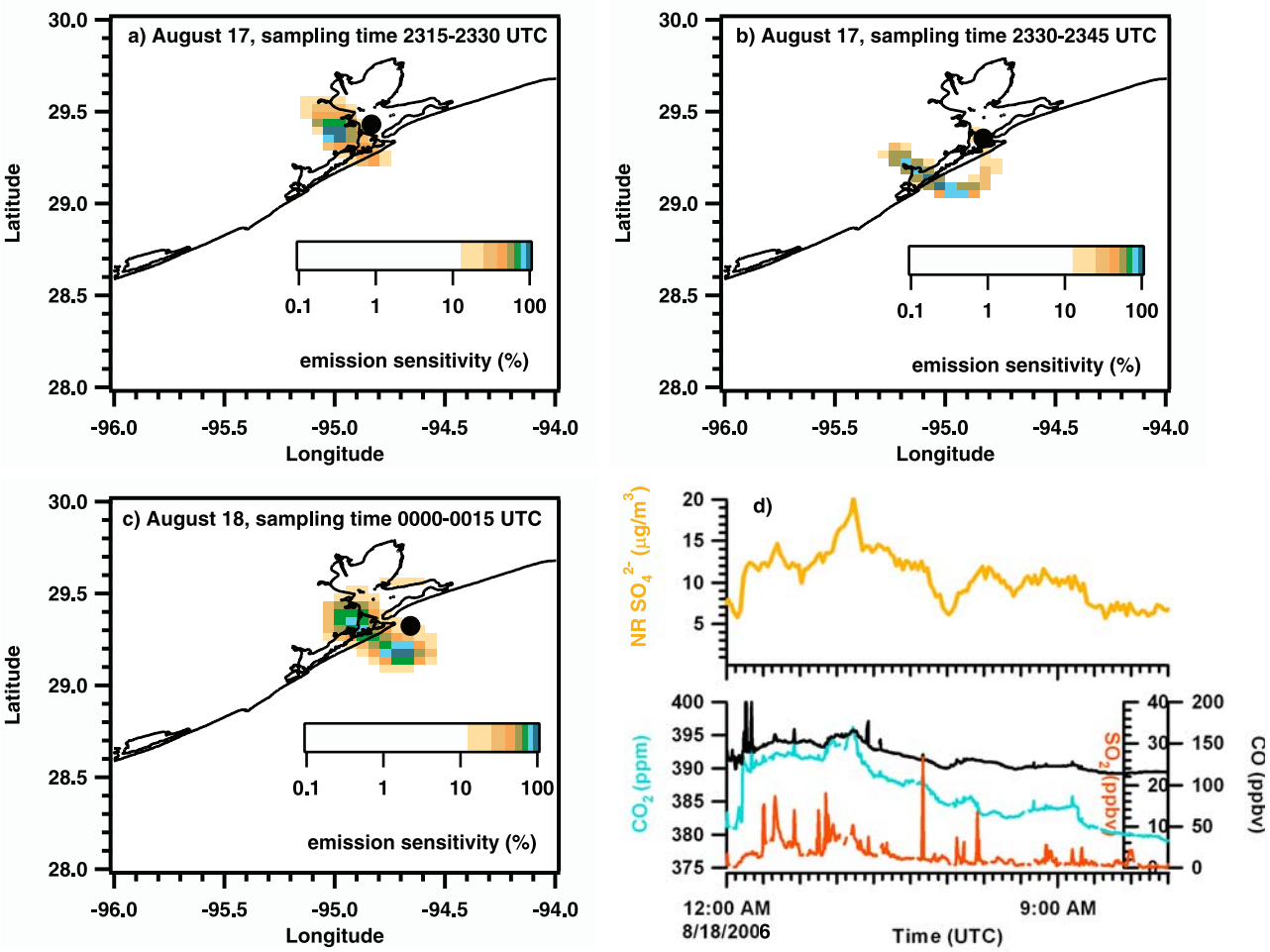

Figure 4. (a, b, c) Footprint emission sensitivities from the WRF-FLEXPART transport model initialized between 2330 and 0015 UTC on 18 August. RHB position is indicated by the black circles. (d) Time series of SO_2, CO, CO_2, and NR sulfate for the time period immediately following the wind shift on 18 August at 0000 UTC.

sulfate, but are less structured than the SO_2 trace. These data indicate a shift from the oxidized urban/industrial plume of Houston to a sulfate-rich plume associated with a significant SO_2 source. Several sources of SO_2 in the area surrounding Galveston Bay and Houston, and mixtures of these sources, might account for the observed sulfate and SO_2 concentrations. Among these, the W. A. Parish power plant on the southwest edge of the Houston area emits substantial amounts of SO_2 [*Brock et al.*, 2003]. Marine vessels have also been shown to be a significant source of SO_2 and sulfate aerosols in the Gulf of Mexico under southeasterly flow [*Bates et al.*, 2008], and might have contributed to the high load of sulfate observed on 18 August later in the day under southeasterly winds.

3.3. Long-Range Transport of Aerosols From the Ohio River Valley

[25] On 2 September at approximately 2100 UTC the submicron extinction coefficient increased abruptly to 90 Mm^{-1} and the concentration of SO_4^{2-} doubled from 5 to 10 $\mu g\ m^{-3}$ while POM remained near 5 $\mu g\ m^{-3}$ (Figure 5a). These conditions of high aerosol loads persisted for 59 h until 0800 UTC on 5 September over which period RHB sampled in an area extending 50 miles along the coast and up to 10 miles out in the Gulf. Aerosol optical depth exceeded 0.3 during this period, and subjectively, visibility was diminished. The observed aerosol properties along with the duration and extent of the event suggest that it was probably associated with long-range transport from a regional-scale source [*Quinn and Bates*, 2003]. Nearly invariant mixing ratios of both CO (160 ppb) and O_3 (65–70 ppb) measured on RHB suggest that contributions from local emissions were minor, except for a 3-h period on 3 September around 1200 UTC (not included in the analysis) when local sources were sampled.

[26] The aerosol associated with this event (Figure 5b) was highly scattering ($\omega = 0.93$) and moderately hygroscopic ($\gamma = 0.66$). Sulfate aerosols dominated the sub-1-μm mass ($F_{POM} = 0.37$) while the organic mass that was present was highly oxygenated ($F_{OOA} = 0.9$). The average $\mathring{A}\sigma_{ep}$ and $\mathring{A}\sigma_{ep\_ambient}$ values were 2.0 and 1.8, respectively.

[27] The FLEXPART transport model indicates that the air sampled by RHB throughout this period was transported from the northeast and had been over the Ohio River Valley

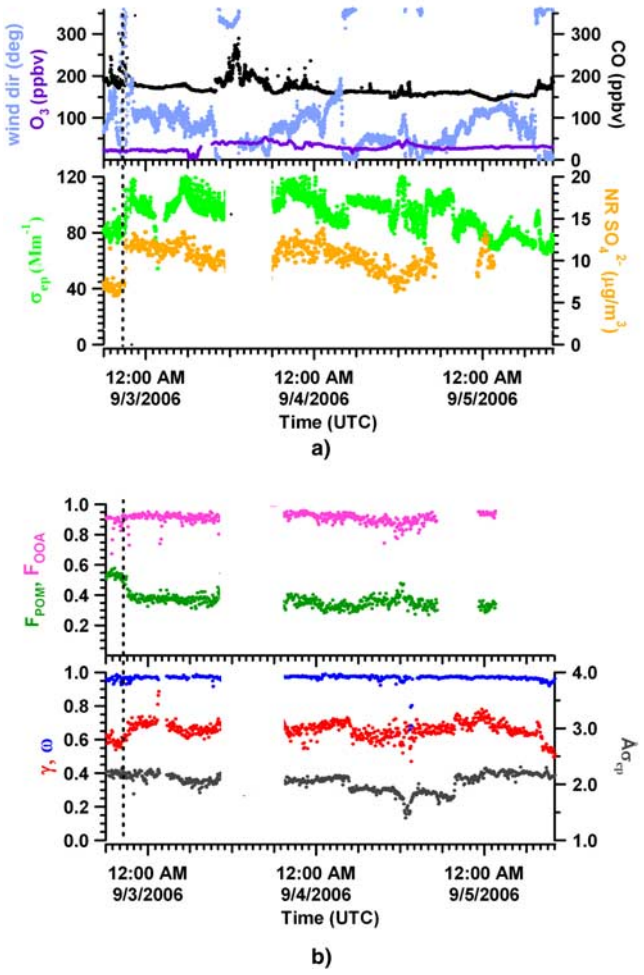

Figure 5. (a) Time series of CO, O_3, 25% RH σ_{ep}, wind direction, and sulphate during long-range transport event from the Ohio River Valley. The dashed line shows the beginning of the event. (b) Time series of γ, ω, Åσ_{ep}, F_{POM}, and F_{OOA} for this event.

(ORV) 3 to 4 days earlier (Figure 6). Clearly, the air might also have been exposed to further emissions during transport from the ORV region to Texas. While elevated SO_2 concentrations (and sulfate levels) are typical of coastal/inland Texas where coal fired power plants are widespread [*Bates et al.*, 2008], such local emissions would not have the time to fully oxidize given the relatively short transport time to RHB ($\sim$1 day), and are inconsistent with the observed spatial and temporal invariance of the aerosol properties. The dominance of sulfate particles during this event is therefore consistent with transport from the extremely large sources of SO_2 in the ORV region, which total $\sim 12 \times 10^6$ kg/d in the summer season [*Brock et al.*, 2008].

[28] To summarize the results presented so far and emphasize the differences in the optical and chemical properties among the selected cases, the data are presented as histograms of the frequency of occurrence of γ, ω, F_{POM} and F_{OOA} (Figure 7). As pointed out earlier, the fresh traffic emissions have the lowest values of γ, ω and F_{OOA}. Aerosols from more aged Houston urban/industrial sources sampled in Galveston bay on 14, 15, 16 and 17 August had progressively larger values of γ and ω. Such changes were correlated with increase in F_{OOA} (larger OOA fraction), whereas F_{POM} values were similar among these air masses ($\sim$0.5). Finally, the sulfate-dominated aerosols exhibited a high γ (>0.65), highly scattering character ($\omega > 0.9$), high sulfate fraction ($F_{POM} < 0.4$), and higher degree of oxidation of the organic components ($F_{OOA} > 0.8$) compared with most of the locally influenced aerosols.

4. Discussion

4.1. Dependence of Aerosol Hygroscopic Behavior on Chemical Composition

[29] The relationship between fraction of organic material (F_{POM}) and aerosol hygroscopic behavior (γ) for the cases discussed so far is depicted in Figure 8. The TexAQS-GoMACCS data covered a broad range of both γ and F_{POM} values: some of the air masses covered larger ranges in the

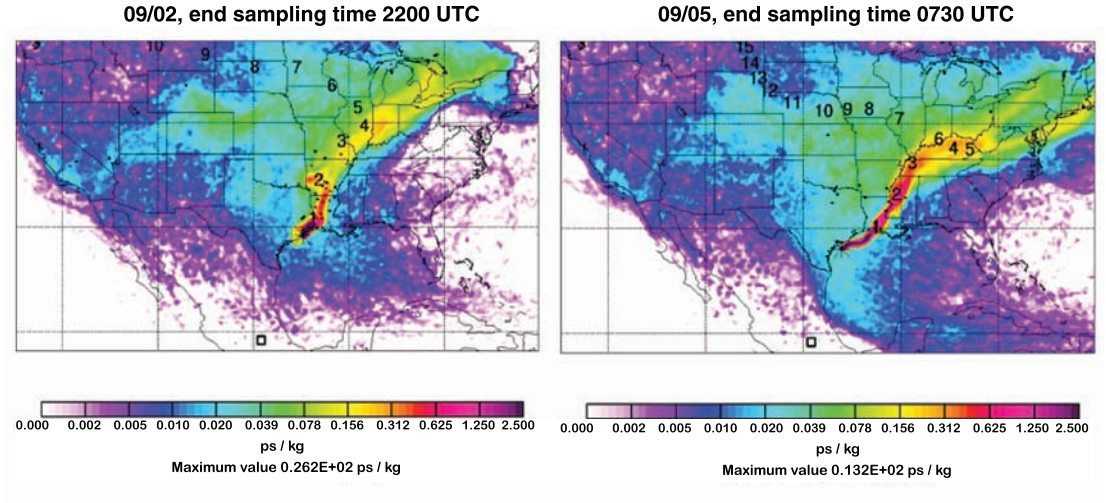

Figure 6. FLEXPART footprint emission sensitivities initialized at the location of the RHB at the (left) beginning and (right) end of the Ohio River Valley transport event. Numbers indicate the number of days of transport for the centroid location of the modeled particles.

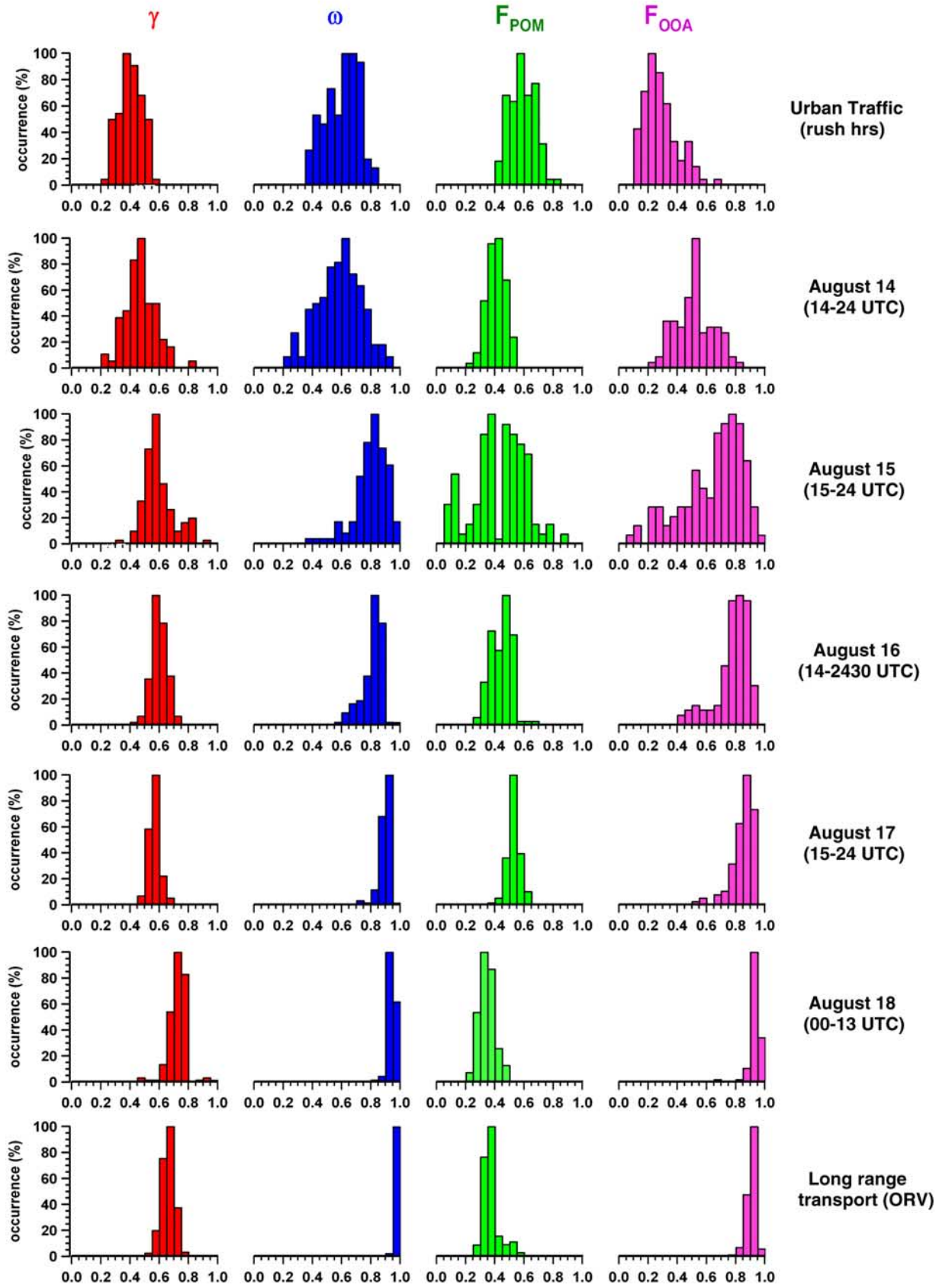

Figure 7. Histograms of the percentage frequency of occurrence of 5-min averaged values of γ, ω, F_{POM}, and F_{OOA} for the aerosol types discussed in the current study.

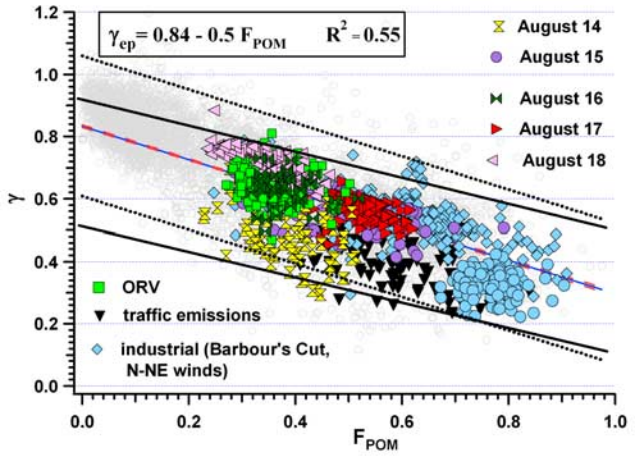

Figure 8. The γ as a function of F_{POM} for each discussed aerosol type. The gray circles represent the entire TexAQS-GoMACCS data set. The blue line is a linear fit to the data, while the red dashed lines are the 95% confidence levels for the fit and the black dotted lines are the 95% prediction bands. The solid lines represent the theoretical boundaries for the γ-F_{POM} relationship predicted using Mie theory.

POM fraction than in the γ values (such as the aerosols sampled in Galveston Bay on 17 and 18 August). Moderately hygroscopic aerosols ($\gamma \sim 0.5$–0.6, such as those observed in some of the Galveston Bay air masses) had a considerable amount of nonrefractory organic material, between 40 and 60%. Even for the most hygroscopic aerosols, the fraction of organics relative to organics and sulfate was at least 30%.

[30] As discussed earlier, the lowest F_{POM} and highest γ values were measured in Galveston Bay on 18 August, as well as during the episode of long-range transport from the ORV. However, even higher γ values may be found in the TexAQS-GoMACCS data set (gray circles). In general, the points on the top left of Figure 8, where $\gamma > 0.8$ and $F_{POM} < 0.25$, are associated with samples taken in the Gulf of Mexico in relatively clean marine air. In contrast, values of $\gamma < 0.4$ are mostly marine vessel emissions, which have been discussed elsewhere [*Lack et al.*, 2009]. Finally, we report data from when RHB sampled on 10 different days in Barbours Cut under northeasterly flow, i.e., downwind of diverse sources in the industrial ship channel and surroundings. These industrial-dominated aerosols had the largest variability in F_{POM} values (between 0.4 and 0.9), and generally low γ, between 0.3 and 0.6.

[31] The linear least squares regression to the TexAQS-GoMACCS data set (coefficients $\pm$ 1σ standard deviation) yields

$$\gamma_{ep} = 0.84(\pm 0.007) - 0.5(\pm 0.017) * F_{POM}. \quad (8)$$

This result is very similar to that obtained from the ACE-ASIA and ICARTT data sets [*Quinn et al.*, 2005] with γ calculated using light scattering coefficients measured with a TSI nephelometer

$$\gamma_{sp} = 0.9(\pm 0.003) - 0.6(\pm 0.01) * F_{POM}. \quad (9)$$

The TexAQS-GoMACCS data set is also well contained with very few outliers in the theoretical γ -F_{POM} parameterization boundaries (Figure 8, solid black lines) derived using both Mie theory-based sensitivity calculations [*Quinn et al.*, 2005] and results from $f\sigma_{ep}(RH)$ laboratory studies [*Baynard et al.*, 2006].

[32] To further explore the relationship between the chemical composition of the aerosols and the γ - F_{POM} parameterization, the data are presented as a function of the degree of SO_2 oxidation to form sulfate, F_{SO4} (Figure 9 and Table 2) and the degree of apparent acidity, or equivalence ratio ER (Figure 10 and Table 2). Relatively lower F_{SO4} (indicating a smaller fractional conversion of SO_2 into sulfate) and higher ER (indicating more neutralization of the sulfate by ammonium) were generally associated with higher F_{POM} and lower γ. Most of the air masses sampled in Galveston bay had relatively low F_{SO4} values suggesting the effects of recent emissions of SO_2. These local emissions may mask the presence of older, more oxidized aerosols from sources further upwind. The highest values of F_{SO4} were present during the long-range transport of ORV pollutants, and during sampling of SO_2-rich but chemically processed air measured on 18 August (section 3.2). Some interesting findings emerge from the combined information of degree of relative sulfur oxidation and degree of neutralization by ammonium. For example, the sulfate aerosols sampled on 18 August after 0000 UTC were more acidic (ER = 0.4) than the ORV aerosols (ER = 0.53), the latter perhaps reflecting the influence of continental sources of NH_3 during transport.

[33] Overall, what emerges from this analysis is a consistent picture of the way the optical properties vary with the chemistry of the aerosols. The variations in the relative amount of POM and sulfate mass fraction for typical ambient aerosol mixtures can explain most of the observed variability in γ. This result suggests that the γ-F_{POM} relationship is robust and broadly applicable in a systematic way to parameterize the bulk composition dependence of the aerosol hygroscopic behavior of both local and regional aerosols. It is also worth investigating the extent to which the chemical composition of our specific cases agrees with the chemical properties of the aerosols in the air mass categories discussed by *Bates et al.* [2008]. For instance, we find that the results

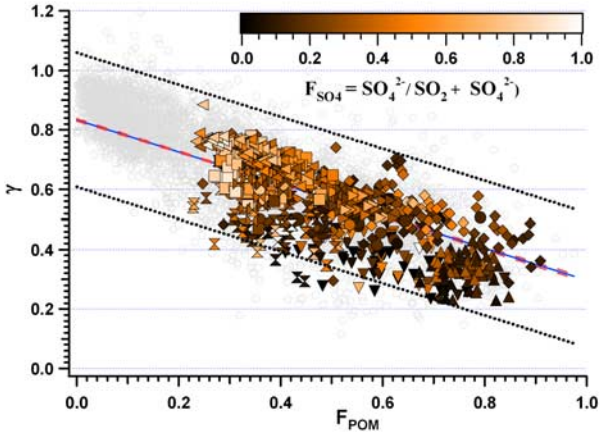

Figure 9. As in Figure 8 but color coded by the fraction of sulfate oxidation F_{SO4}.

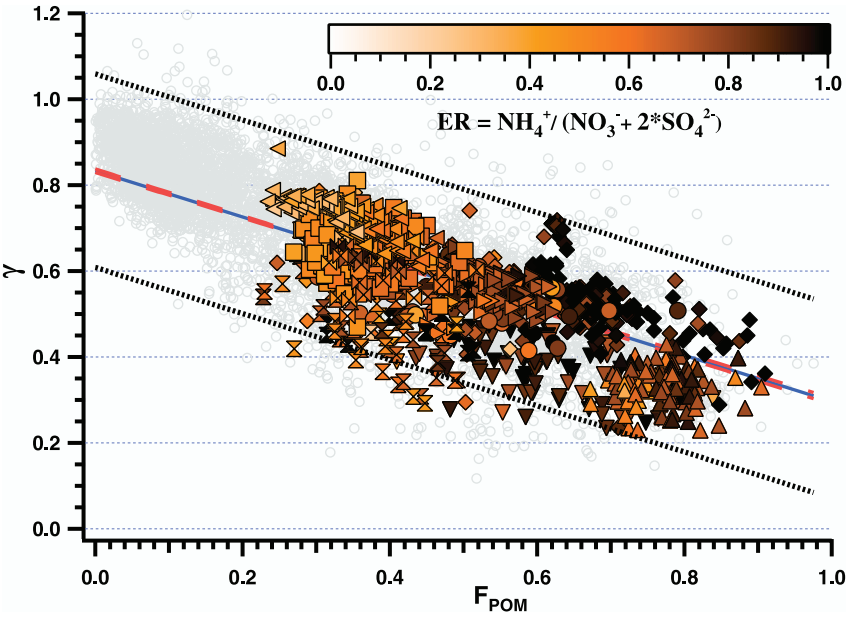

Figure 10. As in Figure 8 but color coded by degree of apparent acidity or equivalence ratio, ER.

obtained for the traffic emissions, with hydrophobic, absorbing, HOA-dominated aerosols and CO enhancement during the morning hours (Figure 2) are consistent with the morning composition as measured in inland locations under southerly flow, or "Category 2" of *Bates et al.* [2008]. The evolution of O_3, F_{POM} and F_{OOA} for the air masses sampled in Galveston Bay between 14 and 17 August (Figure 3) is also consistent with the diurnal variation of the Category 2 aerosols [*Bates et al.*, 2008, Figure 11 (bottom)], which is partly explained by variation in mixing height during the day. Finally, the long-range transport event from sulfur-rich ORV sources occurring under northerly synoptic flow was an extraordinary case of regional aerosol fumigation. Indeed, the aerosol commonly sampled under northerly flow during TexAQS-GoMACCS, i.e., "Category 3" of *Bates et al.* [2008], was mainly composed of OOA-dominated organics rather than sulfate.

4.2. Estimates of Direct Radiative Forcing by Aerosols and Uncertainty Analysis

[34] Uncertainties in aerosol optical properties and the difficulties in resolving the spatial and temporal variability of such properties continue to limit precise quantification of the direct radiative forcing (DRF) by aerosols [*IPCC*, 2007]. Estimates of anthropogenic aerosol DRF based on experimental data are desirable to both evaluate the overall DRF uncertainty due to current aerosol property measurements and provide valuable information for radiative transfer models. The aerosol optical measurements collected during TexAQS-GoMACCS are used to calculate the DRF for the aerosol types discussed in the present study. We calculate the change in upwelling radiation at the top of atmosphere (TOA) as an estimate of the instantaneous forcing (ΔF_R) locally induced by the measured aerosols. Although this approach is much simplified compared to full radiative transfer models, the parameterized method is useful to examine the sensitivity of DRF to the variability and uncertainty in the measured aerosol optical properties.

[35] ΔF_R was calculated using the formula adapted from *Haywood and Shine* [1995] and *Chylek and Wong* [1995] for partially absorbing aerosols,

$$\Delta F_R = -D S_o T^2 (1 - Ac)\omega\beta AOD \times \left\{(1-R)^2 - (2R/\beta)[(1/\omega) - 1]\right\}, \quad (10)$$

where the particle single scattering albedo (ω), the aerosol optical depth (AOD), and the average up-scatter fraction (β) are the measured aerosol optical parameters. The up-scatter fraction β, the light scattered back in the atmosphere, depends on the hemispheric backscatter fraction b, or the ratio of angular corrected backscatter coefficient to the total scattering coefficient. On RHB, b was measured using a TSI nephelometer at 550 nm and 60% RH [*Quinn et al.*, 2004]. Following *Anderson et al.* [1999], we compute β using a simple empirical relationship based on the Henyey-Greenstein phase function [*Wiscombe and Grams*, 1976],

$$\beta = 0.082 + 1.85\,b - 2.79\,b^2. \quad (11)$$

We assume a fractional day length (D) of 0.5, a solar constant (So) of 1366 W/m^2 [*Dewitte et al.*, 2004], a transmittance of the atmosphere above the aerosol layer (T) of 0.76 and an albedo of the underlying ocean surface (R) of 0.05 [*Russell et al.*, 2002]. R values calculated by taking into account changes in solar zenith angles (SZA) and wind speed following *Jin et al.* [2004] showed little variation from an R of 0.05. The calculations were performed for clear-sky conditions, or $Ac = 0$.

[36] Given the recognized importance of accounting for aerosol water uptake in radiative forcing calculations [*Bates et al.*, 2006], ΔF_R was calculated using both ω and $\omega_{ambient}$ (ΔF_R and $\Delta F_{R\_ambient}$, respectively) to describe the sensitivity of aerosol DRF due to changes in ω values. The other optical parameters used in the forcing calculation such as β

Table 3. Value and Absolute Uncertainty of the TOA Forcing Calculated at 25% RH and Ambient RH[a]

	Traffic Emissions	Galveston Bay, 1	Galveston Bay, 2	Galveston Bay, 3	Galveston Bay, 4a	Galveston Bay, 4b	ORV	Industrial
ω ($\delta\omega$)	0.60 (0.02)	0.56 (0.022)	0.80 (0.010)	0.81 (0.010)	0.89 (0.0055)	0.94 (0.0030)	0.93 (0.0035)	0.87 (0.0065)
ω_{ambient} ($\delta\omega_{\text{ambient}}$)	0.72 (0.019)	0.65 (0.025)	0.86 (0.010)	0.88 (0.0085)	0.93 (0.0050)	0.97 (0.0020)	0.98 (0.0014)	0.92 (0.0056)
AOD (δAOD)	0.15 (0.015)	0.20 (0.015)	0.25 (0.015)	0.30 (0.015)	0.30 (0.015)	0.30 (0.015)	0.55 (0.015)	0.30 (0.015)
β ($\delta\beta$)	0.3 (0.050)	0.3 (0.050)	0.3 (0.050)	0.3 (0.050)	0.3 (0.050)	0.3 (0.050)	0.24 (0.050)	0.3 (0.050)
ΔF_R ($\delta\Delta F_R$)	−3.8 (0.66)	−8.5 (0.86)	−19.4 (1.2)	−23.2 (1.5)	−27.2 (1.6)	−29.4 (1.6)	−36.2 (2.4)	−23.3 (1.5)
$\Delta F_{R\_\text{ambient}}$ ($\delta\Delta F_{R\_ambient}$)	−6.9 (0.72)	−11.1 (0.95)	−21.6 (1.3)	−26.7 (1.5)	−28.9 (1.6)	−30.7 (1.6)	−40.5 (2.4)	−26.7 (1.5)

[a]The 25% RH and Ambient RH are ΔF_R and $\Delta F_{R\_ambient}$, respectively. The average value and the absolute uncertainty of the parameters used in the calculations are also shown.

change only slightly with respect to RH [*Kotchenruther et al.*, 1999]. Note that all the ω values were determined from measurements made at 532 nm, whereas the other optical parameters (b and AOD) are at 550 nm; this difference in λ is small and again it can be neglected.

[37] Table 3 lists the average values and absolute uncertainty of the parameters used to derive ΔF_R (equation (10)). The calculated $\omega_{ambient}$ values are up to 0.1 units higher than the measured ω, with the largest changes occurring for the aerosols with $\omega < 0.7$, consistent with *Bates et al.* [2006]. Such variations are significant because they are larger than the uncertainties in the ω values measured in this study, $\delta\omega <$ 1%, for ω between 0.98 and 0.5. For the $\omega_{ambient}$ values, $\delta\omega_{ambient}$ is between 0.1% and 7% over the same range (0.98−0.5) owing to larger uncertainties for σ_{ep} at ambient RH.

[38] Typical b values for TexAQS-GoMACCS were ∼0.15, which translates into β values of approximately 0.3. For the case of long-range transport of sulfate from the ORV region, the measured b was 0.1, resulting in a β of 0.24. The uncertainty in β ($\delta\beta$) is estimated as 0.05 based on uncertainty values of b reported for continental aerosols [*Anderson et al.*, 1999]. The AOD measured at the time closest to the each observed aerosol event was used for the calculation of ΔF_R. The measured AOD ranged between 0.15 and 0.55, and has an estimated uncertainty, δAOD, of 0.015. AOD values above 0.3 reflect significant aerosol burden in the column and are typical of highly polluted regions [*Quinn and Bates*, 2003; *Ramanathan et al.*, 2007]. In general, the AOD during TexAQS-GoMACCS was ∼0.2 during relatively cleaner southerly flow and >0.4 under northerly flow conditions. We do not have information on the vertical structure of aerosol amount and composition during high-AOD periods. However, under northerly flow conditions the planetary boundary layer was often well mixed during the day up to ∼1200 m and in situ surface measurements are likely representative of the boundary layer.

[39] The ΔF_R and $\Delta F_{R\_ambient}$ values and their respective uncertainties ($\delta\Delta F_R$ and $\delta\Delta F_{R\_ambient}$) are also reported in Table 3. For all aerosol types the calculated forcing is negative indicating a cooling effect. For the majority of the air masses examined here the forcing lies between −20 and −30 W/m^2. The greatest calculated cooling (−36.2 W/m^2) is associated with the sulfate-rich aerosols transported from the ORV. These findings are quantitatively consistent with those reported from large-scale plumes which are advected downwind of the North American, Indian and Asian continents and which contribute to a significant reduction of radiation at the surface, or dimming effect [*Ramanathan et al.*, 2007]. The magnitude of the forcing that we calculated depends most strongly on AOD rather than on ω, for example, the most negative ΔF_R occurs for the air masses with the largest AOD and not the highest ω. This is consistent with *McComiskey et al.* [2008] who showed that in full radiative transfer models the forcing estimates are most sensitive to AOD rather than to ω when all else is held constant. The $\delta\Delta F_R$ values are within ±2 W/m^2, or 5−7%; uncertainties become significant where ΔF_R is small, for example, for the traffic emissions (−3.8 ± 0.66 W/m^2, or 17%). The $\Delta F_{R\_ambient}$ are up to 5 W/m^2 lower than the correspondent ΔF_R values owing to generally higher $\omega_{ambient}$, and indicate greater radiative cooling from hydrated aerosols, as expected [*Garland et al.*, 2007]. The smallest

increase in cooling due to aerosol water uptake is associated with the aerosols from traffic emissions, while the greatest increase in cooling occurs for the sulfate rich aerosols. For all the cases with $\omega > 0.8$ (common value for atmospheric aerosols), the average percentage increase in ω to $\omega_{ambient}$ is 5%, leading to an increase in forcing of ~10%. Hence, a relatively small percentage changes in ω (often hidden behind large uncertainties within ω estimates) can propagate to a much larger percentage change in forcing. *McComiskey et al.* [2008] showed that in most situations the uncertainty in DRF is due to the uncertainty in ω values, indicating that improvements in determining ω especially at ambient RH conditions will lead to the largest reductions in the overall uncertainty in DRF. Incorporating the information of the measured aerosol hygroscopic properties in the forcing expression clearly provides more realistic DRF estimates and helps quantify the sensitivity of the atmospheric radiative balance to changes in the aerosol optical properties due to water uptake.

[40] Our results based on the simplified radiative calculation show that uncertainties in ΔF_R are not small, but they can be held below ~20% even for moderately absorbing aerosols ($\omega \sim 0.6$) if $\delta\omega$ is $\leq$5% and ΔF_R values are >10 W/m^2. However, relative uncertainties can become much larger for very strongly absorbing aerosols and at low AODs. Currently, optical property measurements from CRD and PAS result in lower uncertainty estimates of ω than do those obtained from combination of other instruments such as the TSI nephelometer and the particle soot absorption photometer (PSAP) for comparable time resolution and ω levels (P. Massoli et al., Uncertainty in light scattering measurements by nephelometer: results from laboratory studies and implications for ambient measurements, submitted to *Aerospace Science and Technology*, 2009). Continued improvements in precision and accuracy in the determination of ω would further reduce the overall uncertainty in DRF from radiative transfer models that must also accommodate uncertainties related to aerosol spatial/temporal resolution [*Bates et al.*, 2006] and from satellite-based measurements that typically hold large uncertainties [*Anderson et al.*, 2005; *Yu et al.*, 2006].

5. Summary and Conclusions

[41] The hygroscopic, optical and chemical properties of aerosol particles were measured on board the NOAA *RV R. H. Brown* during the 2006 TexAQS-GoMACCS campaign in the Gulf of Mexico. Aerosol light extinction (σ_{ep}, Mm^{-1}) and absorption (σ_{ap}, Mm^{-1}) coefficients were measured by CRD and PAS, respectively. The particle single scattering albedo (ω) was calculated at 532 nm from the combination of σ_{ep} and σ_{ap} with an uncertainty of <0.01 at 25% RH for submicron aerosols. The RH dependence of extinction was parameterized using a previously developed γ formulation, i.e., correlation of γ with the fraction of submicrometer organic mass relative to organic and sulfate (F_{POM}). The TexAQS-GoMACCS data covered a broad spectrum of γ and F_{POM} values, and their correlation was consistent with results obtained from previous data sets in diverse environments [*Quinn et al.*, 2005]. The wide range of aerosol properties encountered during the experiment serve to validate the generality of the γ parameterization for describing aerosol hygroscopic behavior in a simple manner.

[42] Portions of the TexAQS-GoMACCS data set containing unique aerosol characteristics from identifiable sources were selected for further analysis. Aerosols from traffic emissions, sampled during morning rush hours in the shallow boundary layer (0600–0900 local time), were hydrophobic and light absorbing ($\gamma = 0.39$ and $\omega = 0.60$), and the organic fraction was mostly hydrocarbon-like ($F_{\mathrm{OOA}} = 0.28$). Aerosols properties in Galveston Bay during the daytime photochemical production of ozone (1000–1800 local time) were variable as a result of combined effect of sources, oxidation state and mixing; in general, more hygroscopic and light-scattering aerosols corresponded to higher F_{OOA} for similar values of F_{POM}. The role of the region's complex transport processes in shaping the aerosol properties was evident on 18 August when a sulfate-rich, hygroscopic aerosol was brought to RHB in Galveston Bay, probably from sources in the southwest Houston area. An exceptional case of multiday, regional fumigation from sulfate aerosol sources in the Ohio River valley (ORV) showed how long-range transport can greatly affect visibility, air quality and climate over a large distant region. Aerosols sampled in Barbours Cut south of the Houston ship channel, dominated by nearby industrial and shipping sources, showed a large variability in properties; however, in general the particles were hydrophobic, absorbing, and rich in POM.

[43] The optical measurements collected during the field study (ω, AOD, b) were used to estimate the instantaneous forcing (ΔF_R) locally induced at the TOA. Relatively small changes in ω led to significant changes in forcing, especially in some sensitive ω ranges or for small values of ΔF_R. The ability to determine the RH dependence of optical properties is critical for realistic prediction of aerosol behavior at ambient humidity levels. Furthermore, the ability to determine changes in aerosol optical properties with small uncertainties, and their changes with changing RH, is necessary to permit accurate predictions of aerosol direct radiative forcing.

[44] **Acknowledgments.** The authors thank the officers and crew of the NOAA RV *Ronald H. Brown*, D. Hamilton, and D. Coffman for their support. We thank D. Hamilton for performing the AOD measurements during TexAQS-GoMACCS. P.M. thanks C. A. Brock for helpful comments on the manuscript and A. McComiskey, W. Angevine, and G. J. Frost for useful discussions. We thank J. Meagher, F. Fehsenfeld, and A. R. Ravishankara for programmatic support. This project was funded by the NOAA Climate and Global Change Program, the NOAA Office of Oceanic and Atmospheric Research, the NOAA Health of the Atmosphere Program, and the Texas Air Quality Study. Certain commercial equipment, instruments, or materials are identified in this article in order to adequately specify the experimental procedure. Such identification does not imply recognition or endorsement by the National Oceanic and Atmospheric Administration, nor does it imply that the material or equipment identified are necessarily the best available for the purpose.

References

Allen, D. T., and M. Fraser (2006), An overview of the Gulf coast aerosol research and characterization study: The Houston fine particulate matter super site, *J. Air Waste Manage. Assoc.*, *56*, 456–466.

Anderson, T. L., D. Covert, J. Wheeler, J. Harris, K. Perry, B. Trost, D. Jaffe, and J. Ogren (1999), Aerosol backscatter fraction and single scattering albedo: Measured values and uncertainties at a coastal station in the Pacific Northwest, *J. Geophys. Res.*, *104*(D21), 26,793–26,807, doi:10.1029/1999JD900172.

Anderson, T. L., et al. (2005), An "A-Train" strategy for quantifying direct climate forcing by anthropogenic aerosols, *Bull. Am. Meteorol. Soc.*, *86*(12), 1795–1809, doi:10.1175/BAMS-86-12-1795.

Ångström, A. (1929), On the atmospheric transmission of sun radiation and on dust in the air, *Geogr. Ann.*, *11*, 156–166, doi:10.2307/519399.

Banta, R. M., C. J. Senff, T. B. Ryerson, J. Nielsen-Gammon, L. S. Darby, R. J. Alvarez, S. P. Sandberg, E. J. Williams, and M. Trainer (2005), A bad air day in Houston, *Bull. Am. Meteorol. Soc.*, *86*(5), 657–669, doi:10.1175/BAMS-86-5-657.

Bates, T. S., D. J. Coffman, D. S. Covert, and P. K. Quinn (2002), Regional marine boundary layer aerosol size distributions in the Indian, Atlantic, and Pacific oceans: A comparison of INDOEX measurements with ACE-1, ACE-2, and Aerosols99, *J. Geophys. Res.*, *107*(D19), 8026, doi:10.1029/2001JD001174.

Bates, T. S., et al. (2006), Aerosol direct radiative effects over the northwest Atlantic, northwest Pacific, and North Indian oceans: Estimates based on in-situ chemical and optical measurements and chemical transport modeling, *Atmos. Chem. Phys.*, *6*, 1657–1732.

Bates, T. S., et al. (2008), Layer aerosol chemistry during TexAQS/GoMACCS 2006: Insights into aerosol sources and transformation processes, *J. Geophys. Res.*, *113*, D00F01, doi:10.1029/2008JD010023.

Baynard, T., R. M. Garland, A. R. Ravishankara, M. A. Tolbert, and E. R. Lovejoy (2006), Key factors influencing the relative humidity dependence of aerosol light scattering, *Geophys. Res. Lett.*, *33*, L06813, doi:10.1029/2005GL024898.

Baynard, T., A. Pettersson, E. Lovejoy, S. Brown, D. Lack, P. Massoli, H. Osthoff, S. Ciciora, B. Dube, and A. R. Ravishankara (2007), Design and application of a pulsed cavity ring-down aerosol extinction spectrometer for field measurements, *Aerosol Sci. Technol.*, *41*(4), 447–462, doi:10.1080/02786820701222801.

Berner, A., C. Lurzer, F. Pohl, O. Preining, and P. Wagner (1979), The size distribution of the urban aerosol in Vienna, *Sci. Total Environ.*, *13*, 245–261, doi:10.1016/0048-9697(79)90105-0.

Brock, C. A., et al. (2003), Particle growth in urban and industrial plumes in Texas, *J. Geophys. Res.*, *108*(D3), 4111, doi:10.1029/2002JD002746.

Brock, C. A., et al. (2008), Sources of particulate matter in the northeastern United States in summer: 2. Evolution of chemical and microphysical properties, *J. Geophys. Res.*, *113*, D08302, doi:10.1029/2007JD009241.

Chylek, P., and J. Wong (1995), Effect of absorbing aerosols on global radiation budget, *Geophys. Res. Lett.*, *22*(8), 929–931, doi:10.1029/95GL00800.

Clarke, A., et al. (2007), Biomass burning and pollution aerosol over North America: Organic components and their influence on spectral optical properties and humidification response, *J. Geophys. Res.*, *112*, D12S18, doi:10.1029/2006JD007777.

de Gouw, J. A., et al. (2005), Budget of organic carbon in a polluted atmosphere: Results from the New England Air Quality Study in 2002, *J. Geophys. Res.*, *110*, D16305, doi:10.1029/2004JD005623.

Dewitte, S., D. Crommelynck, S. Mekaoui, and A. Joukoff (2004), Measurement and uncertainty of the long-term total solar irradiance trend, *Sol. Phys.*, *224*, 209–216, doi:10.1007/s11207-005-5698-7.

Doherty, S. J., P. K. Quinn, A. Jefferson, C. M. Carrico, T. L. Anderson, and D. Hegg (2005), A comparison and summary of aerosol optical properties as observed in situ from aircraft, ship, and land during ACE-Asia, *J. Geophys. Res.*, *110*, D04201, doi:10.1029/2004JD004964.

Doran, C., J. D. Fast, J. C. Barnard, A. Laskin, Y. Desyaterik, and M. K. Gilles (2008), Applications of Lagrangian dispersion modeling to the analysis of changes in the specific absorption of elemental carbon, *Atmos. Chem. Phys.*, *8*, 1377–1389.

Garland, R. M., A. R. Ravishankara, E. R. Lovejoy, M. A. Tolbert, and T. Baynard (2007), Parameterization for the relative humidity dependence of light extinction: Organic-ammonium sulfate aerosol, *J. Geophys. Res.*, *112*, D19303, doi:10.1029/2006JD008179.

Gassó, S., et al. (2000), Influence of humidity on the aerosol scattering coefficient and its effect on the upwelling radiance during ACE-2, *Tellus, Ser. B*, *52*, 546–567.

Haywood, J. M., and K. P. Shine (1995), The effect of anthropogenic sulfate and soot aerosol on the clear sky planetary radiation budget, *Geophys. Res. Lett.*, *22*(5), 603–606, doi:10.1029/95GL00075.

Imhof, D., et al. (2006), Aerosol and NO_x emission factors and submicron particle number size distributions in two road tunnels with different traffic regimes, *Atmos. Chem. Phys.*, *6*, 2215–2230.

Intergovernmental Panel on Climate Change (2007), *Climate Change 2007: The Physical Science Basis. Contribution of Working Group I to the Fourth Assessment Report of the Intergovernmental Panel on Climate Change*, edited by S. Solomon et al., Cambridge Univ. Press, Cambridge, U. K.

Jayne, J. T., D. C. Leard, X. Zhang, P. Davidovits, K. A. Smith, C. E. Kolb, and D. R. Worsnop (2000), Development of an aerosol mass spectrometer for size and composition analysis of submicron particles, *Aerosol Sci. Technol.*, *33*(1–2), 49–70, doi:10.1080/027868200410840.

Jin, Z., T. P. Charlock, W. L. Smith Jr., and K. Rutledge (2004), A parameterization of ocean surface albedo, *Geophys. Res. Lett.*, *31*, L22301, doi:10.1029/2004GL021180.

Kanakidou, M., et al. (2005), Organic aerosol and global climate modeling: A review, *Atmos. Chem. Phys.*, *5*, 1053–1123.

Kleinman, L. I., P. H. Daum, D. G. Imre, Y.-N. Lee, L. J. Nunnermacker, S. R. Springston, J. Weinstein-Lloyd, and J. Rudolph (2002), Ozone production rate and hydrocarbon reactivity in 5 urban areas: A cause of high ozone concentration in Houston, *Geophys. Res. Lett.*, *29*(10), 1467, doi:10.1029/2001GL014569.

Knobelspiesse, K. D., et al. (2003), Sun-pointing-error correction for sea deployment of the Microtops II handheld Sun photometer, *J. Atmos. Oceanic Technol.*, *20*, 767, doi:10.1175/1520-0426(2003)20<767:SPECFS>2.0.CO;2.

Kotchenruther, R. A., P. V. Hobbs, and D. A. Hegg (1999), Humidification factors for atmospheric aerosols off the mid-Atlantic coast of the United States, *J. Geophys. Res.*, *104*(D2), 2239–2251, doi:10.1029/98JD01751.

Lack, D. A., E. Lovejoy, T. Baynard, A. Pettersson, and A. Ravishankara (2006), Aerosol absorption measurement using photoacoustic spectroscopy: Sensitivity, calibration, and uncertainty developments, *Aerosol Sci. Technol.*, *40*(9), 697–708, doi:10.1080/02786820600803917.

Lack, D. A., B. Lerner, C. Granier, T. Baynard, E. R. Lovejoy, P. Massoli, A. R. Ravishankara, and E. Williams (2008), Light absorbing carbon emissions from commercial shipping, *Geophys. Res. Lett.*, *35*, L13815, doi:10.1029/2008GL033906.

Lack, D. A., et al. (2009), Particulate emissions from commercial shipping: Chemical, physical, and optical properties, *J. Geophys. Res.*, *114*, D00F04, doi:10.1029/2008JD011300.

Lohmann, U., and J. Feichter (2005), Global indirect aerosol effects: A review, *Atmos. Chem. Phys.*, *5*, 715–737.

Malm, W. C., and S. M. Kreidenweis (1997), The effects of models of aerosol hygroscopicity on the apportionment of extinction, *Atmos. Environ.*, *31*, 1965–1976, doi:10.1016/S1352-2310(96)00355-X.

Malm, W. C., et al. (2005), Hygroscopic properties of an organic-laden aerosol, *Atmos. Environ.*, *39*, 4969–4982, doi:10.1016/j.atmosenv.2005.05.014.

McComiskey, A., S. E. Schwartz, B. Schmid, H. Guan, E. R. Lewis, P. Ricchiazzi, and J. A. Ogren (2008), Direct aerosol forcing: Calculations form observables and sensitivities to inputs, *J. Geophys. Res.*, *113*, D09202, doi:10.1029/2007JD009170.

Mircea, M., et al. (2005), Importance of the organic aerosol fraction for modeling aerosol hygroscopic growth and activation: A case study in the Amazon Basin, *Atmos. Chem. Phys.*, *5*, 3111–3126.

Nessler, R., E. Wintergartner, and U. Baltensperger (2005), Effect of humidity on aerosol light absorption and its implication for extinction and the single scattering albedo illustrated for a site in the lower free troposphere, *J. Aerosol Sci.*, *36*(8), 958–972, doi:10.1016/j.jaerosci.2004.11.012.

Quinn, P. K., and T. S. Bates (2003), North American, Asian, and Indian haze: Similar regional impacts on climate?, *Geophys. Res. Lett.*, *30*(11), 1555, doi:10.1029/2003GL016934.

Quinn, P. K., D. J. Coffman, T. S. Bates, T. L. Miller, J. E. Johnson, E. J. Welton, C. Neusüss, M. Miller, and P. Sheridan (2002), Aerosol optical properties during INDOEX 1999: Means, variabilities, and controlling factors, *J. Geophys. Res.*, *107*(D18), 8020, doi:10.1029/2000JD000037.

Quinn, P. K., et al. (2004), Aerosol optical properties measured on board the *Ronald H. Brown* during ACE-Asia as a function of aerosol chemical composition and source region, *J. Geophys. Res.*, *109*, D19S01, doi:10.1029/2003JD004010.

Quinn, P. K., et al. (2005), Impact of particulate organic matter on the relative humidity dependence of light scattering: A simplified parameterization, *Geophys. Res. Lett.*, *32*, L22809, doi:10.1029/2005GL024322.

Ramanathan, V., F. Li, M. V. Ramana, P. S. Praveen, D. Kim, C. E. Corrigan, and H. Nguyen (2007), Atmospheric brown clouds: Hemispherical and regional variations in long-range transport, absorption, and radiative forcing, *J. Geophys. Res.*, *112*, D22S21, doi:10.1029/2006JD008124.

Russell, P. B., et al. (2002), Comparison of aerosol single scattering albedos derived by diverse techniques in two North Atlantic experiments, *J. Atmos. Sci.*, *59*, 609, doi:10.1175/1520-0469(2002)059<0609:COASSA>2.0.CO;2.

Ryerson, T. B., et al. (2003), Effect of petrochemical industrial emissions of reactive alkenes and NO_x on tropospheric ozone formation in Houston, Texas, *J. Geophys. Res.*, *108*(D8), 4249, doi:10.1029/2002JD003070.

Seibert, P., and A. Frank (2004), Source-receptor matrix calculation with a Lagrangian particle dispersion model in backward mode, *Atmos. Chem. Phys.*, *4*, 51–63.

Stohl, A., M. Hittenberger, and G. Wotawa (1998), Validation of the Lagrangian particle dispersion model FLEXPART against large scale tracer experiments, *Atmos. Environ.*, *32*, 4245–4264, doi:10.1016/S1352-2310(98)00184-8.

Stohl, A., C. Forster, A. Frank, P. Seibert, and G. Wotawa (2005), Technical note: The Lagrangian particle dispersion model FLEXPART version 6.2, *Atmos. Chem. Phys.*, *5*, 2461–2474.

Trainer, M., D. D. Parrish, P. D. Goldan, J. Roberts, and F. C. Fehsenfeld (2000), Review of observation-based analysis of the regional factors influencing ozone concentrations, *Atmos. Environ.*, *34*, 2045–2061, doi:10.1016/S1352-2310(99)00459-8.

Tucker, S. C., et al. (2009), Doppler lidar estimation of mixing height using turbulence, shear, and aerosol profiles, *J. Atmos. Oceanic Technol.*, doi:10.1175/2008JTECHA1157.1, in press.

Wang, J., and S. T. Martin (2007), Satellite characterization of urban aerosols: Importance of including hygroscopicity and mixing state in the retrieval algorithms, *J. Geophys. Res.*, *112*, D17203, doi:10.1029/2006JD008078.

Wiscombe, W. J., and G. W. Grams (1976), The backscattered fraction in two-stream approximations, *J. Atmos. Sci.*, *33*, 2440–2451, doi:10.1175/1520-0469(1976)033<2440:TBFITS>2.0.CO;2.

Yu, H., et al. (2006), A review of measurement-based assessment of aerosol direct radiative effect and forcing, *Atmos. Chem. Phys.*, *6*, 613–666.

Zhang, Q., M. R. Alfarra, D. R. Worsnop, J. D. Allan, H. Coe, M. R. Canagaratna, and J. L. Jimenez (2005), Deconvolution and quantification of hydrocarbon-like and oxygenated organic aerosols based on aerosol mass spectrometry, *Environ. Sci. Technol.*, *39*, 4938–4952, doi:10.1021/es048568l.

Zhang, R., W. Lei, X. Tie, and P. Hess (2004), Industrial emissions cause extreme urban ozone diurnal variability, *Proc. Natl. Acad. Sci. U. S. A.*, *101*, 6346–6350, doi:10.1073/pnas.0401484101.

T. S. Bates and P. K. Quinn, Pacific Marine Environment Laboratory, NOAA, 7600 Sand Point Way, Seattle, WA 98115, USA.

T. Baynard, Lockheed Martin Coherent Technologies, 135 South Taylor Avenue, Louisville, CO 80027, USA.

J. Brioude, D. A. Lack, B. M. Lerner, P. Massoli, S. C. Tucker and E. J. Williams, Chemical Sciences Division, Earth System Research Laboratory, NOAA, 325 Broadway, Boulder, CO 80309, USA. (pmassoli@aerodyne.com)

A. Stohl, Department of Regional and Global Pollution Issues, Norwegian Institute for Air Research, N-2027 Kjeller, Norway.